Global biosphere primary productivity changes during the past eight glacial cycles

Yang Ji-Woong [1, *], Brandon Margaux [1, 2], Landais Amaëlle [1], Duchamp-Alphonse Stéphanie [2], Blunier Thomas [3], Prié Frédéric [1], Extier Thomas [1]

[1] Laboratoire des Sciences du Climat et de l'Environnement/Institut Pierre-Simon Laplace, Université Paris Saclay/CEA/CNRS/UVSQ, Gif-sur-Yvette, France.
[2] Géosciences Paris-Saclay, Université Paris Saclay, Orsay, France.
[3] Niels Bohr Institute, University of Copenhagen, København N, Denmark.

* Corresponding author : Ji-Wong Yang, email address : ji-woong.yang@lsce.ipsl.fr

Abstract :

Global biosphere productivity is the largest uptake flux of atmospheric carbon dioxide (CO_2), and it plays an important role in past and future carbon cycles. However, global estimation of biosphere productivity remains a challenge. Using the ancient air enclosed in polar ice cores, we present the first 800,000-year record of triple isotopic ratios of atmospheric oxygen, which reflects past global biosphere productivity. We observe that global biosphere productivity in the past eight glacial intervals was lower than that in the preindustrial era and that, in most cases, it starts to increase millennia before deglaciations. Both variations occur concomitantly with CO_2 changes, implying a dominant control of CO_2 on global biosphere productivity that supports a pervasive negative feedback under the glacial climate.

Main Text: Atmospheric carbon dioxide (CO_2) is a potent greenhouse gas that, together with orbital changes, is a primary determinant of Earth's global climate. Measurements of the CO_2 mixing ratio of air trapped in ice cores over the last 800 thousand years (ka) reveal clear glacial-interglacial cycles (*1, 2*) showing a good correlation with global sea-level changes (*3*). The Southern Ocean (SO) is thought to have played a major role in these CO_2 variations through changes in sea-ice cover, overturning circulation and biological productivity (*4–7*), and there is growing evidence that the terrestrial vegetation may be a significant contributor as well (e.g., *8*). Nevertheless, there are periods where CO_2 concentration decouples from sea-level, particularly during full glacial periods when CO_2 shows relatively stable or slightly rising trends while sea-level continues to decline (*9, 10*).

To explain this CO_2 evolution during full glacial times, Galbraith and Eggleston (*10*) hypothesized a negative feedback by which global photosynthesis becomes limited by low atmospheric CO_2 concentrations, prohibiting further CO_2 drawdown. This hypothesis has not been proven yet by observations since the reconstructions of past biosphere productivity are based on geochemical (e.g., organic and inorganic biomarkers) and micropaleontological (e.g., pollen, coccolith, diatoms) data from sediment archives which provide indirect and only qualitative reconstructions (e.g., *11*). Furthermore, they show sometimes contrasting changes making it difficult to estimate global variations. As an example, terrestrial vegetation records (e.g., arboreal pollen fraction) show a drastic decrease during glacial times, while phytoplankton indicators (mainly TOC and alkenones) in the Subantarctic Zone (SAZ), a key part of the SO (*6, 12*), suggest intensified marine productivity.

The above limitations can be alleviated by using measurements of the triple isotope composition (^{16}O, ^{17}O, and ^{18}O) of atmospheric oxygen (O_2), a marker of global gross productivity expressed in O_2 flux (*13*). The triple isotopic composition of O_2 is primarily affected by O-isotope exchange with CO_2 during photochemical reactions in the stratosphere and biological reactions of photosynthesis and respiration (*13, 14*). The heavy isotopes (^{17}O and ^{18}O) are discriminated relative to the light one (^{16}O) in a mass-dependent way during most biological reactions. On the contrary, O_2-CO_2 isotope exchange in the stratosphere fractionates in a mass-independent manner (*13–15*). Accordingly, to estimate relative contribution of biosphere and stratosphere fluxes, the ^{17}O anomaly of O_2 is defined as: $^{17}\Delta \equiv \ln(\delta^{17}O + 1) - \lambda_{ref} \cdot \ln(\delta^{18}O + 1)$ (*16*), where λ_{ref} is the mass-dependent reference slope of 0.516 calculated from the modern O_2 isotope fractionations within the global biospheric cycle (*16, 17*). By definition, tropospheric $^{17}\Delta$ is not much modified by the mass-dependent fractionation within biosphere. Closed terrarium experiments showed that without stratospheric exchange, biospheric processes induce a positive $^{17}\Delta$ signal relative to the present atmosphere (*13*). In contrast, the stratospheric air measurements from rocket (*15*), aircraft (e.g., *20, 21*), and balloons (e.g., *21, 22*) observed a highly positive $^{17}\Delta$ of CO_2 as a result of photolysis of O_2 and ozone (O_3) and atomic O exchange with CO_2 (*23*), which is counterbalanced by a slight depletion of $^{17}\Delta$ of the O_2 reservoir in the stratosphere ($^{17}\Delta_{strat}$) because of small abundance (mixing ratio) of O_3 relative to O_2 (*24*). In the present atmosphere, the input of positively fractionated $^{17}\Delta$ from the biosphere ($^{17}\Delta_{bio}$) is equilibrated by a massive flux of O_2 with slightly negative $^{17}\Delta$ from the stratosphere. The sizes of the two endmember fluxes from the biosphere and the stratosphere hence drive the $^{17}\Delta$ variations, so by knowing magnitudes of the O_2 isotopic fractionations in the stratosphere and O_2 fluxes from the

stratosphere (F_{strat}), $^{17}\Delta$ can be used to reconstruct the gross O_2 flux from Earth biosphere (F_{bio}), or global gross primary productivity in terms of O_2 (GPP-O_2).

Stratospheric influence on tropospheric $^{17}\Delta$ is through different factors including F_{strat}, stratosphere temperature, photochemical reaction rates, and O_3 abundance in the stratosphere. Numerical simulations show that greenhouse gases (predominantly CO_2) play an important role in controlling the above-mentioned changes in the stratosphere (e.g., *25-28*), allowing the stratosphere effect to be scaled to CO_2 changes such that high CO_2 mixing ratio in troposphere induces strong depletion in $^{17}\Delta$ [see (*29*) for more details]. It should be noted that O_2 photolysis in the mesosphere may cause additional fractionation (*30*). However, model simulations suggest that the entrainment of mesospheric air into the stratosphere is small (~0.02%) (*30*), and its effect on the tropospheric $^{17}\Delta$ is expected to be negligible (*29*).

As a consequence, the imprint of the stratospheric mass-independent fractionation is reflected in the general anti-correlation between CO_2 and $^{17}\Delta$. However, CO_2 and $^{17}\Delta$ are not always anti-correlated as they decouple when changes in biosphere productivity occur. For example, Brandon *et al.* (*8*) pointed out that the notable decoupling over Termination V (TV) – Marine Isotope Stage (MIS) 11 interval may be interpreted as an imprint of exceptionally high biosphere productivity. Therefore, the decoupling between CO_2 and $^{17}\Delta$ is the key to infer the past evolution of global biosphere productivity, which provides unique insights into the past global carbon cycle.

The previous ice-core record of $^{17}\Delta$ extends over the last 444.8 ka (*8, 31*). During the last 4 glacial cycles characterized by a large glacial-interglacial amplitude and a periodicity of ~100 ka, the inferred global biosphere productivity was systematically lower during glacial than during interglacial times (*31*). The amplitude of temperature and CO_2 changes over glacial-interglacial transitions was smaller before 450 ka and the glacial periods were shorter than after 450 ka (*2*). Knowing the global biosphere productivity over the period 800–450 ka is hence of uttermost importance to study the interactions between the Earth biosphere and CO_2 level during the glacial-interglacial cycles. Here we extend the $^{17}\Delta$ records back to ~796 ka by analyzing samples from the European Project for Ice Coring in Antarctica Dome C (EDC) ice core (*29*). The data were corrected for the fractionations by gas-loss during ice storage, gravitational settling, and bubble close-off (*29*).

Decoupling between $^{17}\Delta$ and CO_2

The fully corrected EDC $^{17}\Delta$ data are plotted with CO_2 in Fig. 1. We observe a general anti-correlation between CO_2 and $^{17}\Delta$ over the last 796 ka (r = -0.73, Fig. 1G and fig. S2). However, this anti-correlation does not hold true during glacial intervals (Fig. 1. A to C): the moving correlation coefficients between CO_2 and $^{17}\Delta$ show a significant positive correlation in the middle of glacial intervals of MISs 6, 8, 10, 12, 16, and 18 (Fig. 1E). Indeed, CO_2 concentrations show stable- or slightly increasing trends while $^{17}\Delta$ signals gradually increase to glacial maxima (Fig. 1C). We illustrate this decoupling between $^{17}\Delta$ and CO_2 through the $^{17}\Delta$ offset (Fig. 1D) which is the difference between the ice-core $^{17}\Delta$ and a hypothetical $^{17}\Delta$ ($^{17}\Delta_{arb}$) purely driven by stratospheric fractionation (Fig. 1C and fig. S3) (*32*). Negative $^{17}\Delta$ offsets (orange in Fig. 1D, 1G, and 1I) result from reduced biosphere productivity while positive ones (green in Fig. 1D, 1G, and 1I) can be explained by enhanced biosphere productivity. The negative offsets (reduced

productivity) are found at earlier stages of glacial periods, while the positive ones (increased productivity) prevail from later stages of glacial to interglacial periods.

GPP-O$_2$ reconstructions using box models

To obtain a more quantitative assessment of past changes in global biosphere productivity, we applied two different box models [TB model (*31*) and AL model (*33*)] describing triple O$_2$ isotope budgets in biosphere, troposphere, and stratosphere. Assuming steady-state, both models calculate the biosphere O$_2$ flux so that the biosphere input of $^{17}\Delta$ is balanced by O$_2$ flux from the stratosphere, which is estimated from the CO$_2$ concentration in the troposphere (*13*). The different assumptions made by the two models and their limitations are described in SM (*29*).

The reconstructed GPP-O$_2$ from the two different models are presented in Fig. 2B in terms of the ratio between the global biosphere O$_2$ flux of the past (F$_{bio,t}$) and the global biosphere O$_2$ flux of the preindustrial condition (F$_{bio,PST}$). Although the two model results are not necessarily identical, they share common features that confirm our qualitative inferences based on $^{17}\Delta$ offset (Fig. 1): (i) they reveal clear glacial (low productivity) - interglacial (high productivity) cycles during the last 796 ka, (ii) the GPP-O$_2$ minima during each glacial period occurred under intermediate sea-level, and concomitantly with glacial CO$_2$ minima (mid-glacial stage) (Fig. 2, A and B), (iii) following the glacial minima, GPP-O$_2$ increases while global ice volume continues to grow until the glacial maxima (full-glacial stage), millennia before the glacial terminations (Figs. 2B and 3B).

Glacial-Interglacial changes

Both box-model results indicate concomitant GPP-O$_2$ and CO$_2$ minima during each of the 8 glacial intervals (Fig. 2) with glacial productivity minima which are estimated to lie between 55% and 87% of modern. We explore below the possible contributions of marine and terrestrial productivity to this large reduction of global GPP-O$_2$ under glacial times.

The only global compilation of marine sedimentary records of marine productivity that exist for glacial times focuses on the Last Glacial Maximum (LGM) and indicates stronger export production and probably higher marine primary productivity (PP) during the LGM than during the Holocene (*12*). Over the last 800 ka, the very few available marine export production (EP) records suggested to reflect PP reveal spatially different patterns during glacial times. The alkenone concentration at ODP 1090 site located in the SAZ shows an increased PP during glacial periods (*6*), while biogenic barium (Ba/Fe) from ODP 1094 in Antarctic Zone (AZ) of the SO (*34*), and Ba/Al ratio from ODP 882 core in the subarctic Pacific (*35*) indicate reduced PP (Figs. 2G-I). In addition, the Ba/Ti from the core TT013-PC72 in the Equatorial Pacific exhibits no clear G-IG pattern (*36*) (Fig. 2J). None of those records explain our reconstructed lower global GPP-O$_2$ during glacial periods. Global ocean PP in glacial times is difficult to predict and ocean biogeochemical models have shown contrasting results: some predict greater global PP in LGM (*37*), while others represent the opposite (*38*) or no clear change (*39*). On the one hand, a decrease of ocean PP is expected because colder sea surface temperature (SST) reduces the metabolic rate of marine phytoplankton (e.g., *40*), shoaling of overturning circulation reduces the intake of nutrient-rich deep water (*41*) and highly productive continental shelf area are lost by sea-level decline. On the other hand, an increase of ocean PP could arise from greatly enhanced

aeolian dust deposition that supplies iron to high-nutrient low-chlorophyll (HPLC) oceans such as SO (e.g., *6*).

No direct proxies for terrestrial GPP exists but we do have indirect vegetation cover proxies, some of which reflect glacial shrinking and interglacial expansion patterns. Two long-term pollen assembly records in Europe – Tenaghi Phillippon (*42*) and Lake Ohrid (*43*) – clearly indicate a near vanishing arboreal-type pollen (AP) during glacial periods (Fig. 2K). In addition, woodland and mountain forest type vegetations from MD96-2048 core off SE Africa exhibit G-IG variations (*44*) (Fig. 2L). Similar G-IG patterns are observed in biogenic silica records from BDP-96 core from Lake Baikal (*45*) (Fig. 2M).

Several arguments favor a stronger decrease in terrestrial GPP than in marine PP during glacial intervals. Nearly 90 ppm lower CO_2 in glacial atmosphere would have a strong negative fertilizing effect on photosynthesis of terrestrial vegetation (*46, 47*), whereas its impact on marine PP is expected to be minor (*48*). A modelling study using a dynamic global vegetation model (DGVM) shows that a CO_2 increase of 185 to 285 rises by more than a factor of two, the vegetation GPP (*46*). The temperature and precipitation impact on terrestrial GPP are less clear. Although modern observations suggest temperature and precipitation as important controls for terrestrial GPP (*e.g.*, *49*), model studies show that climate change alone (without changes in CO_2) has limited impact on glacial-interglacial vegetation GPP changes (*47, 50*). A glacial sea-level low-stand might have two opposing effects, with the exposure of continental shelves promoting increased amounts of new vegetation (*51, 52*) and ice-sheet expansion prohibiting photosynthesis in the ice-covered area. Previous DGVM simulations suggested that the relative sea-level (RSL) decline would increase LGM vegetation net primary productivity (NPP) by ~8% relative to constant RSL results (*53*). Taken together, it is therefore likely that the G-IG changes in global GPP-O_2 are largely driven by terrestrial productivity, whose evolution is strongly influenced by CO_2.

Glacial productivity changes

The glacial productivity minima occur at mid-glacial stages, followed by the systematic increase in GPP-O_2 from mid- to full-glacial stages. Such increase in productivity between mid and full glacial is not easy to detect from paleoproductivity proxies because of a lack of high-resolution records and/or chronological issues. In the ocean, neither ODP 1090 alkenone concentrations nor ODP 882 Ba/Al records exhibit detectable shift between the two stages, with the exceptions of MISs 6 and 12 (ODP 1090) and MIS 8 (ODP 882) (Figs. 2G and 2I). In parallel, the TT-13-PC72 Ba/Ti record starts to rise several millennia prior to maximum productivity at deglacial terminations (Fig. 2J). In the terrestrial realm, the arboreal pollen fractions at Tenaghi Phillippon, Lake Ohrid, and biogenic silica at Lake Baikal indicate nearly vanished productivity during glacial times, showing no clear trends during the mid- to full-glacial changes (Fig 2, K to M). In contrast, the MD96-2048 pollen assemblage records show that the fractions of woodland and mountain forest species increased in the late-glacial stages during certain glacial intervals such as MISs 6, 8, 10, and 12 (Fig. 2J). Therefore, despite the complexity of comparing our GPP-O_2 records with local records, the GPP-O_2 increase between mid and full glacial is confirmed by some local records.

There are several ways in which the possible contributions of the main potential drivers of GPP-O_2 might help to explain the increasing GPP-O_2 signal between full and mid-glacial stages. As mentioned above, the CO_2 fertilization effect may play a significant role and there is a clear correlation between GPP-O_2 and CO_2 changes over the mid to full glacial stages (Fig. 4). The

observed GPP-O_2 vs CO_2 changes agree with second order fitting of Chen *et al.* (*46*)'s sensitivity simulations (Fig. 4A). However, over MISs 8 and 16, the GPP-O_2 vs CO_2 relationship is slightly different, suggesting that factors other than CO_2 concentration affect the GPP-O_2 evolution during glacial periods (Fig. 4A).

First, the global temperature change between mid and full-glacial stages is minor, as observed from the global air surface temperature (GAST) reconstructions (*54*) and a global sea surface temperature (SST) stack (*9*), which show no warming, or only minor changes (Fig. 3).

Second, RSL reconstructions indicate sea-level declines of 10 to 30 meters between mid- and full-glacial stages in most glacial periods (*55*) (Fig. 3). Recalling that there was an ~8% increase in terrestrial NPP at the LGM for an RSL change of ~120 m (*53, 55*), the sea-level decline between two glacial stages should have only a small effect. Moreover, the comparison between GPP-O_2 and RSL records show no strong relationship (Fig. 4D). Therefore, we consider that the sea-level changes have minor impact on glacial GPP-O_2 changes.

Third, low-latitude hydrological changes could play a role as well, as global vegetation is expected to be shifted southerly during glacial periods due to Northern Hemisphere (NH) ice sheet expansion (e.g., *56*). Climate model experiments for the LGM show an increase in precipitation in Southern Hemisphere (SH) low-latitude regions, such as Amazonia and South Africa, by which modelled vegetation NPP is increased in tropical- and temperate forests compared to present (*47*). Proxies for past evolution of the low latitude water cycle exist such as the Dole effect (DE) i.e., the $\delta^{18}O$ offset between air O_2 and sea water (*14*) and speleothem $\delta^{18}O_{calcite}$ from Chinese caves (*57*). The long DE records (*58*) indicate a mid- to full-glacial enrichment over most glacial periods when GPP-O_2 increases, which implies a further southward shift of the Intertropical Convergence Zone (ITCZ) from mid to full glacial stages (Fig. 4B). This is supported by Chinese caves $\delta^{18}O_{calcite}$ records over MISs 6 and 10 (*57*). Therefore, above evidence suggest that southward shift of the ITCZ at the full-glacial stages might have stimulated terrestrial GPP-O_2.

Finally, marine productivity may also contribute to this GPP-O_2 increase, especially in the SO, where the primary productivity is usually limited by iron (e.g., *46*). This iron limitation is alleviated by greater dust deposition into the SAZ, caused by stronger wind, together with glacial aridity and meridional shift of westerly winds (*6*). However, the changes in EDC dust flux are not systematically positively correlated with GPP-O_2 increases (Fig. 4C): the full-glacial increases in EDC dust flux are observed only in MISs 6, 12, and 16, where the GPP-O_2 increases are relatively small (Fig. 4C).

Our $^{17}\Delta$ data provide a complete view of global biosphere productivity evolution during the last 800 ka which confirms the pervasive glacial (low GPP) – interglacial (high GPP) cycles, and demonstrate an important feature of intra-glacial GPP shift. The GPP reconstructions and proxy evidence discussed here suggest that much of the GPP-O_2 changes over glacial-interglacial cycles and between two glacial stages are dominantly attributable to CO_2 changes and that, in both cases, terrestrial GPP might have played an important role. Our findings also demonstrate the close interactions of global photosynthesis with CO_2 over the last 800 ka, providing observational evidence of the pervasive negative feedback between global photosynthesis and CO_2 (*10*).

References and Notes

1. D. Lüthi *et al*., Nature 453, 379–382 (2008). doi:10.1038/nature06949

2. B. Bereiter *et al*., Geophys. Res. Lett. 42, 542–549 (2015). doi:10.1002/2014GL061957

3. G. L. Foster, E. J. Rohling, Proc. Natl. Acad. Sci. U.S.A. 110, 1209–1214 (2013). doi:10.1073/pnas.1216073110

4. B. B. Stephens, R. F. Keeling, Nature 404, 171-174 (2000). doi:10.1038/35004556

5. D. M. Sigman, M. P. Hain, G. H. Haug, Nature 466, 47-55 (2010). doi:10.1038/nature09149

6. A. Martínez-Garcia *et al*., Paleoceanography 24, PA1207 (2009). doi:10.1029/2008PA001657

7. S. Duchamp-Alphonse *et al*., Nature Commun. 9, 2396 (2018). doi:10.1038/s41467-018-04625-7

8. M. Brandon *et al*., Nat. Commun. 11, 2112 (2020). doi:10.1038/s41467-020-15739-2

9. J. D. Shakun, D. W. Lea, L. E. Lisiecki, M. E. Raymo, Earth Planet. Sci. Lett. 426, 58-68 (2015). doi:10.1016/j.epsl.2015.05.042

10. E. D. Galbraith, S. Eggleston, Nat. Geosci. 10, 295-298 (2017). doi:10.1038/NGEO2914

11. K. B. Averyt, A. Paytan, Paleoceanography 19, PA4003 (2004). doi:10.1029/2004PA001005.

12. K. E. Kohfeld, C. Le Quéré, S. P. Harrison, R. F. Anderson, Science 308, 74-78 (2005). doi:10.1126/science.1105375

13. B. Luz, E. Barkan, M. L. Bender, M. H. Thiemens, K. A. Boering, Nature 400, 547-550 (1999). doi:10.1038/22987

14. M. Bender, T. Sowers, L. Labeyrie, Global Biogeochem. Cycles 8, 363-376 (1994). doi:10.1029/94GB00724

15. M. H. Thiemens, T. Jackson, E. C. Jipf, P. W. Erdman, C. van Egmond, Science 270, 969-972 (1995). doi:10.1126/science.270.5238.969

16. B. Luz, E. Barkan, Geochim. Cosmochim. Acta 69, 1099-1110 (2005). doi:10.1016/j.gca.2004.09.001

17. Recent laboratory incubation studies suggested either lower λ of ~0.510 (*18*) or higher λ of ~0.522 (*19*) during dark respiration, however, sensitivity tests performed with λ of 0.510 and 0.520 lead to $^{17}\Delta$ variations within uncertainty range. See (*29*) for more details.

18. J. L. Ash, H. Hu, L. Y. Yeung, ACS Earth Space Chem. 4, 50-66 (2020). doi:10.1021/acsearthspacechem.9b00230

19. D. A. Stolper, W. W. Fischer, M. L. Bender, Geochim. Cosmochim. Acta 240, 152-172 (2018). doi:10.1016/j.gca.2018.07.039

20. K. A. Boering *et al*., Geophys. Res. Lett. 31, L03109 (2004). doi:10.1029/2003GL018451

21. A. A. Wiegel *et al*., Proc. Natl. Acad. Sci. U.S.A. 110, 17680-17685 (2013). doi:10.1073/pnas,1213082110

22. B. Alexander, M. K. Vollmer, T. Jackson, R. F. Weiss, M. H. Thiemens, Geophys. Res. Lett. 28, 4103-4106 (2001). doi:10.1029/2001GL013692

23. Y. L. Yung, W. B. DeMore, J. P. Pinto, Geophys. Res. Lett. 18, 13-16 (1991). doi:10.1029/90GL02478

24. M. H. Thiemens, M. Lin, Rev. Mineral. Geochem. 86, 35-95 (2021). doi:10.2138/rmg.2021.86.02

25. N. Butchart *et al*., Clim. Dyn. 27, 727-741 (2006). doi:10.1007/s00382-006-0162-4

26. K. P. Shine *et al*., Quart. J. Roy. Meteor. Soc. 129, 1565-1588 (2003). doi:10.1256/qr.02.186.

27. G. Chiodo *et al*., J. Clim. 31, 3893-3907 (2018). doi:10.1175/JCLI-D-17-0492.s1.

28. E. L. Fleming, C. H. Jackman, R. S. Stolarski, A. R. Douglas, Atmos. Chem. Phys. 11, 8515-8541 (2011). doi:10.5194/acp-11-8515-2011

29. Materials and methods are available as supplementary materials.

30. M.-C. Liang, G. A. Blake, B. R. Lewis, Y. L. Yung, Proc. Natl. Acad. Sci. U.S.A. 104, 21-25 (2006). doi:10.1073/pnas.0610009104

31. T. Blunier, M. L. Bender, B. Barnett, J. C. von Fischer, Clim. Past 8, 1509-1526 (2012). doi:10.5194/cp-8-1509-2012

32. $^{17}\Delta_{arb}$ is the expected $^{17}\Delta$ in the troposphere if biosphere (F_{bio} and $^{17}\Delta_{bio}$) remains constant over time, hence it is hypothesized to be affected by the stratosphere only. The stratosphere changes are assumed to be limited by CO_2 (*13*, *33*). $^{17}\Delta_{arb}$ is therefore calculated as tropospheric $^{17}\Delta$ in the steady-state equations S2 and S4 in the 3-box model (AL model) by assuming constant F_{bio} and $^{17}\Delta_{bio}$ [see (*29*) for more details].

33. A. Landais, J. Lathiere, E. Barkan, B. Luz, Global Biogeochem. Cycles 21, GB1025 (2007). doi:10.1029/2006GB002739

34. S. L. Jaccard *et al*., Science 339, 1419-1423 (2013). doi:10.1126/science.1227545

35. S. L. Jaccard, E. D. Galbraith, D. M. Sigman, G. H. Haug, Quat. Sci. Rev. 29, 206-212 (2010). doi:10.1016/j.quascirev.2009.10.007

36. R. W. Murray, C. Knowlton, M. Leinen, A. C. Mix, C. H. Polsky, Paleoceanography and Paleoclimatology 15, 570-592 (2000). doi:10.1029/1999PA000457

37. V. Brovkin, A. Ganopolski, D. Archer, S. Rahmstorf, Paleoceanography 22, PA4202 (2007). doi:10.1029/2006PA001380

38. A. Tagliabue *et al*., Clim. Past 5, 695-706 (2009). doi:10.5194/cp-5-695-2009

39. L. Bopp, K. E. Kohfeld, C. Le Quéré, O. Aumont, Paleoceanography 18, 1046 (2003). doi:10.1029/2002PA000810

40. R. W. Eppley, Fish. Bull. 70, 1063 (1972).

41. J. B. Palter, J. L. Sarmiento, A. Gnanadesikan, J. Simeon, R. D. Slater, Biogeosciences 7, 3549-3568 (2010). doi:10.5194/bg-7-3549-2010

42. P. C. Tzedakis, H. Hooghiemstra, H. Pälike, Quat. Sci. Rev. 25, 3416-3430 (2006). doi:10.1016/j.quascirev.2006.09.002

43. L. Sadori *et al*., Biogeosciences 13, 1423-1437 (2016). doi:10.5194/bg-13-1423-2016

44. L. M. Dupont, T. Caley, I. S. Castaneda, Clim. Past 15, 1083-1097 (2019). doi:10.5194/cp-15-1083-2019

45. A. A. Prokopenko, L. A. Hinnov, D. F. Williams, M. I. Kuzmin, Quat. Sci. Rev. 25, 3431-3457 (2006). doi:10.1016/j.quascirev.2006.10.002

46. W. Chen *et al*., Quat. Sci. Rev. 218, 293–305 (2019). doi:10.1016/j.quascirev.2019.06.003

47. M. N. Woillez *et al.*, Clim. Past 7, 557-577 (2011). doi :10.5194/cp-7-557-2011

48. M. Hein, K. Sand-Jensen, Nature 388, 526-527 (1997). doi:10.1038/41457

49. A. Anav *et al.*, Rev. Geophys. 53, 785-818 (2015). doi:10.1002/2015RG000483

50. M. Martin Calvo, I. C. Prentice, New Phytol. 208, 987-994 (2015). doi:10.1111/nph.13485

51. T. Hanebuth, K. Stattegger, P. M. Grootes, Science 288, 1033-1035 (2000). doi: 10.1126/science.288.5468.1033

52. X. Wang, X. Sun, P. Wang, K. Stattegger, Palaeogeogr. Palaeoclimatol. Palaeoecol. 278, 88-97 (2009). doi:10.1016/j.palaeo.2009.04.008

53. B. A. A. Hoogakker et al., Clim. Past 12, 51-73 (2016). doi:10.5194/cp-12-51-2016

54. C. W. Snyder, Nature 538, 226-228 (2016). doi:10.1038/nature19798

55. R. M. Spratt, L. E. Lisiecki, Clim. Past 12, 1079-1092 (2016). doi:10.5194/cp-12-1079-2016

56. I. C. Prentice, S. P. Harrison, P. J. Bartlein, New Phytol. 189, 988-998 (2011). doi: 10.1111/j.1469-8137.2010.03620.x

57. H. Cheng *et al.*, Nature 534, 640-646 (2016). doi:10.1038/nature18591

58. E. Huang *et al.*, Sci. Adv. 6, eaba4823 (2020). doi:10.1126/sciadv.aba4823

59. M. P. Hain, D. M. Sigman, G. H. Haug, in *Treatise on Geochemistry, Volume 8: The Oceans and Marine Geochemistry*, H. D. Holland, K. K. Turekian, Eds. (Elsevier, ed. 2, 2014), pp. 485-517. doi:10.1016/B978-0-08-095975-7.00618-5

60. T. Blunier, B. Barnett, M. L. Bender, M. B. Hendricks, Global Biogeochem. Cycles 16, 1029 (2002). doi:10.1029/2001GB001460

61. L. E. Lisiecki, M. E. Raymo, Paleoceanography 20, PA1003 (2005). doi:10.1029/2004PA001071

62. L. Bazin *et al.*, Clim. Past 9, 1715-1731 (2013). doi:10.5194/cp-9-1715-2013

63. D. Veres *et al.*, Clim. Past 9, 1733-1748 (2013). doi:10.5194/cp-9-1733-2013

64. F. Lambert, M. Bigler, J. P. Steffensen, M. Hutterli, H. Fischer, Clim. Past 8, 609-623 (2012). doi:10.5194/cp-8-609-2012

65. T. Extier *et al.*, Quat. Sci. Rev. 185, 244-257 (2018). doi:10.1016/j.quascirev.2018.02.008

66. J. -W. Yang *et al.*, Triple isotope composition of O_2 records from EPICA Dome C over 453 – 796 ka, PANGAEA (2022): http://doi.org/10.1594/PANGAEA.xxxxxx.

67. E. Barkan, B. Luz, Rapid Commun. Mass Spectrom. 17, 2809-2814 (2003) doi:10.1002/rcm.1267

68. G. B. Dreyfus *et al.*, Quat. Sci. Rev. 29, 28-42 (2010). doi:10.1016/j.quascirev.2009.10.012

69. M. Suwa, M. L. Bender, Quat. Sci. Rev. 27, 1093-1106 (2008). doi:10.1016/j.quascirev.2008.02.017

70. F. Parrenin *et al.*, Science 339, 1060-1063 (2013). doi:10.1126/science.1226368

71. D. A. Stolper, M. L. Bender, G. B. Dreyfus, Y. Yan, J. A. Higgins, Science 353, 1427-1430 (2016). doi:10.1126/science.aaf5445

72. C. Appenzeller, J. R. Holton, K. H. Rosenlof, J. Geophys. Res. 101, 15071-15078 (1996). doi:10.1029/96JD00821

73. R. A. Berner, Geochim. Cosmochim. Acta 65, 685-694 (2001). doi:10.1016/S0016-7037(00)00572-X

74. H. D. Holland, Geochim. Cosmochim. Acta 66, 3811-3826 (2002). doi:10.1016/S0016-7037(02)00950-X

75. B. Luz, E. Barkan, Science 288, 2028-2031 (2000). doi:10.1126/science.288.5473.2028

76. B. Luz, E. Barkan, Geophys. Res. Lett. 38, L19606 (2011). doi:10.1029/2011GL049138

77. C. Waelbroeck *et al.*, Quat. Sci. Rev. 21, 295-305 (2002). doi:10.1016/S0277-3791(01)00101-9

78. E. Barkan, B. Luz, Rapid Commun. Mass Spectrom. 19, 3737-3742 (2005). doi:10.1002/rcm.2250

79. G. Hoffmann, J. Jouzel, V. Masson, Hydrol. Process. 14, 1385-1406 (2000). doi:10.1002/1099-1085(20000615)14:8<1385::AID-HYP989>3.0.CO;2-1

80. M. R. Badger, S. von Caemmerer, S. Ruuska, H. Nakano, Phil. Trans. R. Soc. Lond. B 355, 1433-1446 (2000). doi:10.1098/rstb.2000.0704

81. Y. Helman, E. Barkan, D. Eisenstadt, B. Luz, A. Kaplan, Plant Physiol. 138, 2292-2298 (2005). doi:10.1104/pp.105.063768

82. A. Angert *et al.*, Global Biogeochem. Cycles 17, 1089 (2003). doi:10.1029/2003GB002056

83. M. Ribas-Carbo *et al.*, Plant Cell Environ. 23, 983-989 (2000). doi:10.1046/j.1365-3040.2000.00607.x

84. R. D. Guy, M. L. Fogel, J. A. Berry, Plant Physiol. 101, 37-47 (1993). doi:10.1104/pp.101.1.37

85. C. B. Field, M. J. Behrenfeld, J. T. Randerson, P. Falkowski, Science 281, 237-240 (1998). doi:10.1126/science.281.5374.237

86. L. M. François, C. Delire, P. Warnant, G. Munhoven, Global Planet. Change 16, 37-52 (1998). doi:10.1016/S0921-8181(98)00005-8

87. F. Joos, S. Gerber, I. C. Prentice, B. L. Otto-Bliesner, P. J. Valdes, Global Biogeochem. Cycles 18, GB2002 (2004). doi:10.1029/2003GB002156

88. M. G. Prokopenko, O. M. Pauluis, J. Granger, L. Y. Yeung, Geophys. Res. Lett. 38, L14603 (2011). doi:10.1029/2011GL047652

89. R. Winkler *et al.*, Clim. Past 8, 1-16 (2012). doi:10.5194/cp-8-1-2012

90. R. F. Keeling, "Development of an interferometric oxygen analyzer for precise measurement of the atmospheric O_2 mole fraction," thesis, Harvard University, Cambridge, MA (1988).

91. S. von Caemmerer, G. D. Farquhar, Planta 153, 376-387 (1981). doi:10.1007/BF00384257

92. M. N. Woillez *et al.*, Clim. Past 10, 1165-1182 (2014). doi:10.5194/cp-10-1165-2014

93. P. Le Mézo, L. Beaufort, L. Bopp, P. Braconnot, M. Kageyama, Clim. Past 13, 759-778 (2017). doi:10.5194/cp-13-759-2017

94. M. Wang, Q. Fu, S. Solomon, R. H. White, B. Alexander, J. Geophys. Res. 125, e2020JD032929 (2020). doi:10.1029/2020JD032929

95. Q. Fu *et al.*, Geophys. Res. Lett. 47, e2019GL086271 (2020). doi :10.1029/2019GL086271

96. M. Abalos *et al.*, Atmos. Chem. Phys. 21, 13571-13591 (2021). doi :10.5194/acp-21-13571-2021

97. S. J. Eichelberger, D. L. Hartmann, Geophys. Res. Lett. 32, L15807 (2005). doi:10.1029/2005GL022924

98. R. R. Garcia. W. J. Randel, J. Atmos. Sci. 65, 2731-2739 (2008). doi :10.1175/2008JAS2712.1

99. C. Kodama, T. Iwasaki, K. Shibata, S. Yukimoto, J. Geophys. Res. 112, D16103 (2007). doi:10.1029/2006JD008219

100. D. Rind, J. Lerner, C. McLinden, J. Geophys. Res. 106, 28061-28079 (2001). doi:10.1029/2001JD000439

101. F. Li, R. S. Stolarski, P. A. Newman, Atmos. Chem. Phys. 9, 2207-2213 (2009). doi:10.5194/acp-9-2207-2009

102. T. G. Shepherd, Atmos. Ocean 46, 117-138 (2008). doi:10.3137/ao.460106

103. S. R. Hall *et al*., Atmos. Chem. Phys. 18, 16809-16828 (2018). doi:10.5194/acp-18-16809-2018

104. K. Lamy *et al*., Atmos. Chem. Phys. 19, 10087-10110 (2019). doi :10.5194/acp-19-10087-2019

105. R. S. Stolarski, A. R. Douglass, P. A. Newman, S. Pawson, M. R. Schoeberl, J. Clim. 23, 28-42 (2010). doi:10.1175/2009JCLI2955.1

Author contributions:

Conceptualization: JWY, MB, AL, SDA

Methodology: AL, MB, FP, JWY

Formal analysis: JWY, TB

Investigation: JWY, AL, MB, SDA, TB, TE

Visualization: JWY, MB

Funding acquisition: JWY, AL, SDA, MB

Project administration: JWY, AL

Resources: AL, FP, TB

Supervision: AL, SDA

Validation: JWY, MB, AL, TB

Writing – original draft: JWY, AL, MB

Writing – review & editing: JWY, AL, SDA, MB, TE, TB

Competing interests: Authors declare no competing interests.

Data and materials availability: New EDC $^{17}\Delta$ data will be made available via PANGAEA repository (*65*).

Supplementary Materials

Materials and Methods

Supplementary Text

Figs. S1 to S10

Tables S1 to S4

References (*67–105*)

Fig. 1. The 800,000-year ice-core composite of $^{17}\Delta$ records. (**A**) Compilation of $^{17}\Delta$ of multiple ice-core records with previously published data (*8, 31, 60*). The new EDC data produced in this study are plotted in blue triangles with 1-sigma uncertainty ranges. The smoothed curve of the compilation record is shown in red solid line. (**B**) Ice-core CO_2 compilation (grey dots) and the smoothed curve (red) (*1, 2*). (**C**) Smoothed $^{17}\Delta$ (black) and $^{17}\Delta_{arb}$ time series (red). (**D**) $^{17}\Delta$ offset between the two-time series in (C). (**E**) 20-ka moving correlation coefficient (blue) and p-values (red) between smoothed $^{17}\Delta$ and $^{17}\Delta_{arb}$ time series in (C). (**F**) LR04 benthic $\delta^{18}O$ stack (*61*). The light- and dark yellow shadings denote the negative and positive offsets within the even-numbered MIS stages as defined by (*61*). (**G**) Scatter plot between $^{17}\Delta$ and CO_2, both smoothed by 11-kyr moving average (fig. S2). The CO_2 composite data in (B) are interpolated to the ages of $^{17}\Delta$ data. The linear regression of CO_2 to $^{17}\Delta_{arb}$ is shown in dark red. At given CO_2, scatter points in the right (green) and the left (orange) to the regression line imply enhanced and reduced F_{bio}, respectively. (**H** and **I**) The enlarged view of (C) and (D) over MIS 16 interval. All of the plots are based on, or transferred to AICC 2012 chronology (*29, 62, 63*).

Fig. 2. Comparison of the reconstructed GPP-O$_2$ with global and regional paleoclimate records. (**A**) Ice-core CO$_2$ composite (*1, 2*) smoothed by 5-ka moving average. (**B**) GPP-O$_2$ reconstructed by AL (blue) and TB (pink) models. For AL model, the dark- and light blue shadings represent 68% and 95% ranges of Monte-Carlo sensitivity solutions (*29*). The TB model solutions for LGM C4 plant contribution of 0.7 (pink) and 0.4 (yellow) are plotted with corresponding curves with the Holocene-LGM ^{17}O anomaly offset of 10 ppm (thin pink and thin yellow, respectively). All the model reconstructions are smoothed by 5-ka moving average. (**C**) RSL reconstruction (*55*). (**D**) GAST anomaly from present (0-5 ka) (*54*). (**E**) Global SST stack (*9*). (**F**) EDC dust flux (*64*) smoothed by 5-ka moving mean. (**G**) Alkenone concentration from ODP 1090 core (*6*). (**H**) Ba/Fe ratio from ODP 1094 core (*20*) smoothed by 5-ka moving average. (**I**) Ba/Al ratio at ODP 882 site (*35*) smoothed by 5-ka moving average. (**J**) Ba/Ti ratio from TT013-PC72 core (*36*). (**K**) Biogenic silica from Lake Baikal (*45*). (**L**) Arboreal pollen fraction from Lake Ohrid (brown) (*43*) and Tenaghi Phillippon (dark green) (*42*). (**M**) Fractional abundances of the pollen end-members at MD96-2048 core, SE Africa (*44*). Yellow shadings indicate the interglacial periods.

Fig. 3. Close-up of GPP-O$_2$ evolution during glacial intervals with different climate proxies. (**A**) Ice-core $\delta^{18}O_{atm}$ composite (dark blue) (*65*) and DE (purple) (*58*). (**B**) GPP-O$_2$ reconstructions using AL and TB model in identical color schemes than in Fig. 2. (**C**) ice-core CO$_2$ composite (*1, 2*). (**D**) RSL re construction (*55*). (**E**) GAST anomaly from present (0-5 ka) (*54*). (**F**) global SST stack (*9*). (**G**) EDC dust flux (*64*). Blue and red shadings indicate the mid- and full-glacial stages, respectively.

5

Fig. 4. Comparison of magnitude of changes in GPP-O$_2$ and potential climatic controls between the two glacial stages. The differences (expressed in Δ) between the average values of the two stages (full-glacial minus mid-glacial stages) as defined in Fig. 3. Both ΔGPP-O$_2$ results from AL (square) and TB (triangle) models are plotted. (**A**) Comparison with CO$_2$ changes. The grey solid line stands for the ΔGPP-O$_2$ predicted by second-order regression of CO$_2$ sensitivity simulations using ORCHIDEE model (*46*), assuming constant ocean productivity and terrestrial-to-marine GPP ratio. The ΔGPP-O$_2$ uncertainties are taken as 16 to 84 percentiles of the Monte-Carlo simulations (n=1000) of 26 sensitivity scenarios. CO$_2$ uncertainties are taken from (*2*). (**B**) Comparison with DE changes (*58*). The positive changes indicate southward displacement of tropical rainbelt. The uncertainties for ΔDE are based on the 1σ errors reported in (*58*). (**C**) Comparison with changes in EDC dust flux (*64*). The positive offset implies stronger iron fertilization on SO during full-glacial stages compared to the mid-glacial. ΔDust flux uncertainty is estimated by assuming the maximum analytical error reported as 10% (*64*). (**D**) Comparison with RSL changes (*55*). The ΔRSL uncertainty is based on the 1σ uncertainty ranges in (*55*).
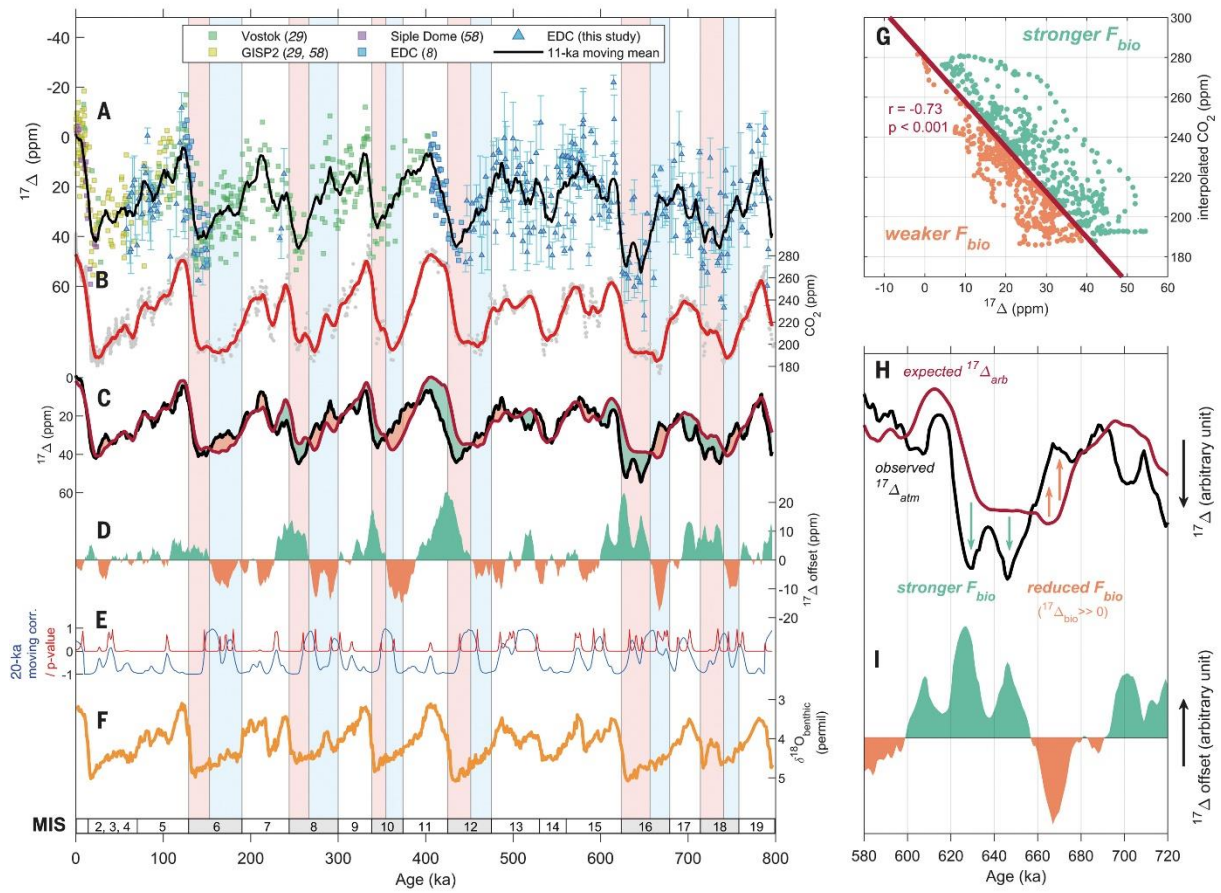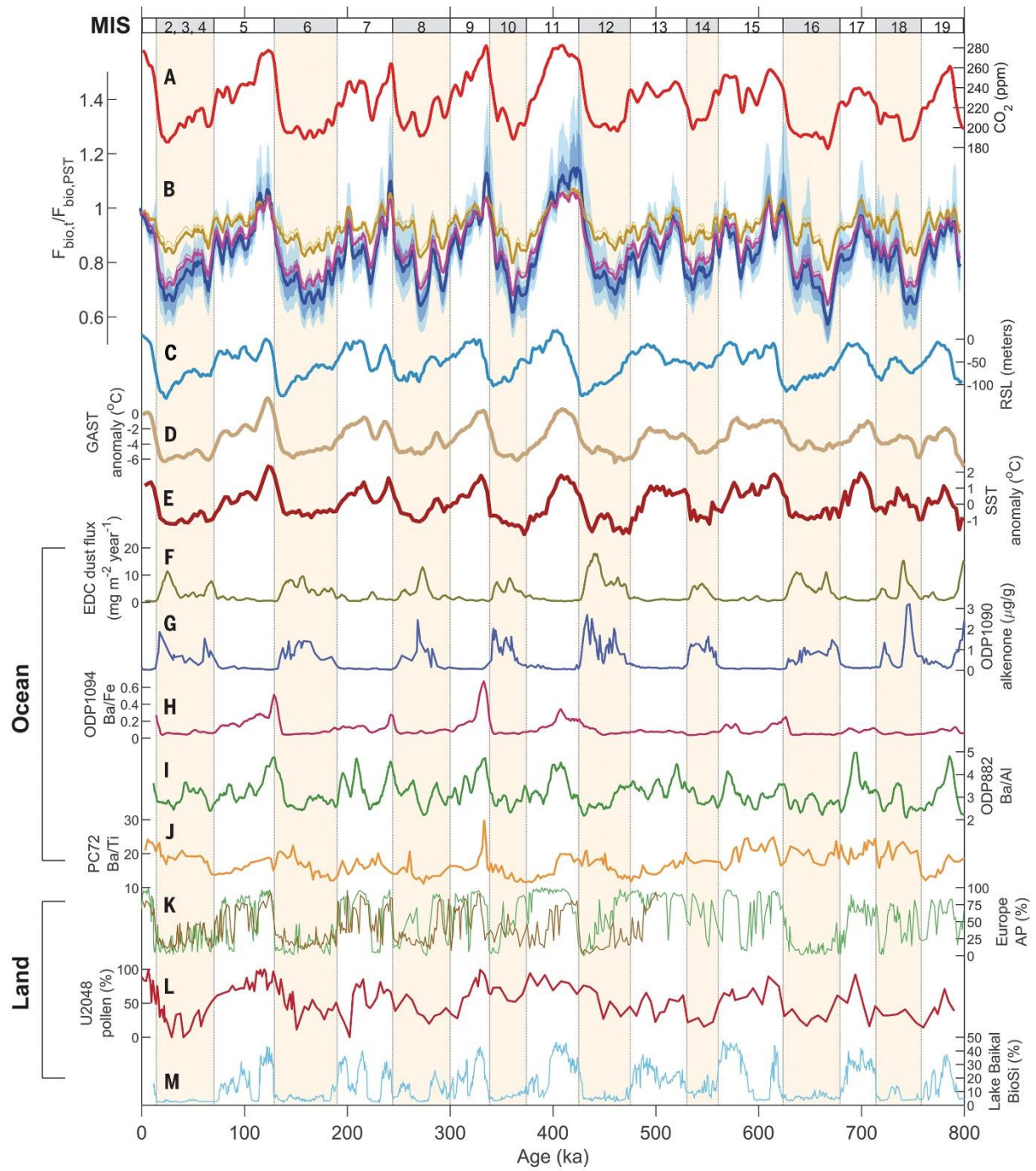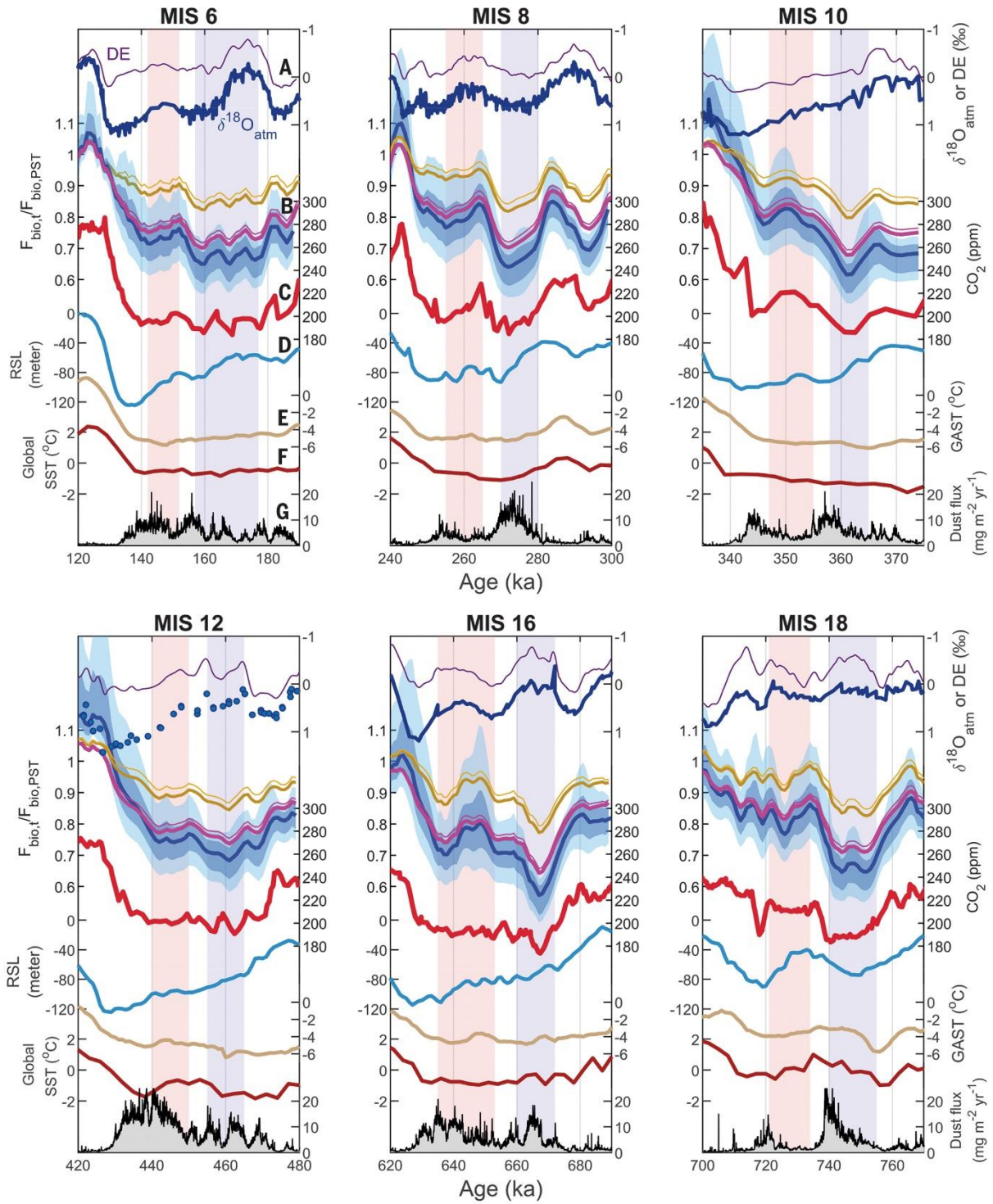
Figure 1

Figure 2

Figure 3

Figure 4